Optik - International Journal for Light and Electron Optics 245 (2021) 167737

Contents lists available at ScienceDirect

Optik

journal homepage: www.elsevier.com/locate/ijleo

Research on evaluation method of stereo vision measurement system based on parameter-driven

Miao Zhang [a], Jiashan Cui [b,*], Fangrui Zhang [b], Ning Yang [c], Yunhui Li [d], Fangyan Li [b], Zhongwen Deng [e]

[a] Beijing Institute of Spacecraft System Engineering, Beijing 100094, China
[b] School of Aerospace Science and Technology, Xidian University, Xi'an 710126, China
[c] Shandong Institute of Space Electronic Technology, Yantai 264670, China
[d] School of Mechatronic Engineering and Automation, Shanghai University, Shanghai 200444, China
[e] Academy of Advanced Interdisciplinary Research, Xidian University, Xi'an, China

ARTICLE INFO

Keywords:
Vision measurement
Stereo vision
Error analysis
Parameter-driven

ABSTRACT

Stereo vision measurement system is widely used in aerospace manufacturing, intelligent robot and other fields because of its unique advantages. However, when using the stereo vision measurement system for measurement, there is no guidance for the parameter configuration of the measurement system for the scene and task constraints, resulting in the stereo vision measurement system cannot play the maximum performance. In this paper, from two aspects of local measurement of camera parameters and global measurement of system parameters, the relevant model is established to analyze the measurement performance of a single independent camera and the performance of the whole stereo vision measurement system. Firstly, the relationship between single camera calibration parameters and measurement accuracy is analyzed; secondly, the relationship between stereo measurement system parameters and measurement accuracy is analyzed; finally, the stereo vision measurement error function is established to guide the design of measurement system parameters. According to the actual measurement experiment, the correctness of the analysis and the accuracy of the established function are verified, it is efficiently used for guiding the parameter design and camera selection of the measurement system in different measurement scene and task.

1. Introduction

In recent years, with the rapid development of stereo vision motion measurement technology, many products have come out and got good application effect [1–3]. This is due to its stable binocular stereo structure and the amount of information obtained, which can more truly and objectively reflect the real world movement of objects. Binocular stereo vision motion measurement technology does not need complex auxiliary equipment, it can determine the structure and motion parameters of the moving target through the amount of information obtained by binocular camera. Because it can independently complete specific measurement tasks, it is widely used in national defense [4], industrial production [5], and modern medical [6] and other fields [7–10]. Such as aircraft attitude control and analysis [11,12], structural vibration test and analysis [13], vehicle collision test [14], visual navigation [15], 3D object modeling and

* Corresponding author.
E-mail address: jscui@xidian.edu.cn (J. Cui).

https://doi.org/10.1016/j.ijleo.2021.167737
Received 25 February 2021; Received in revised form 23 July 2021; Accepted 29 July 2021
Available online 31 July 2021
0030-4026/© 2021 Elsevier GmbH. All rights reserved.

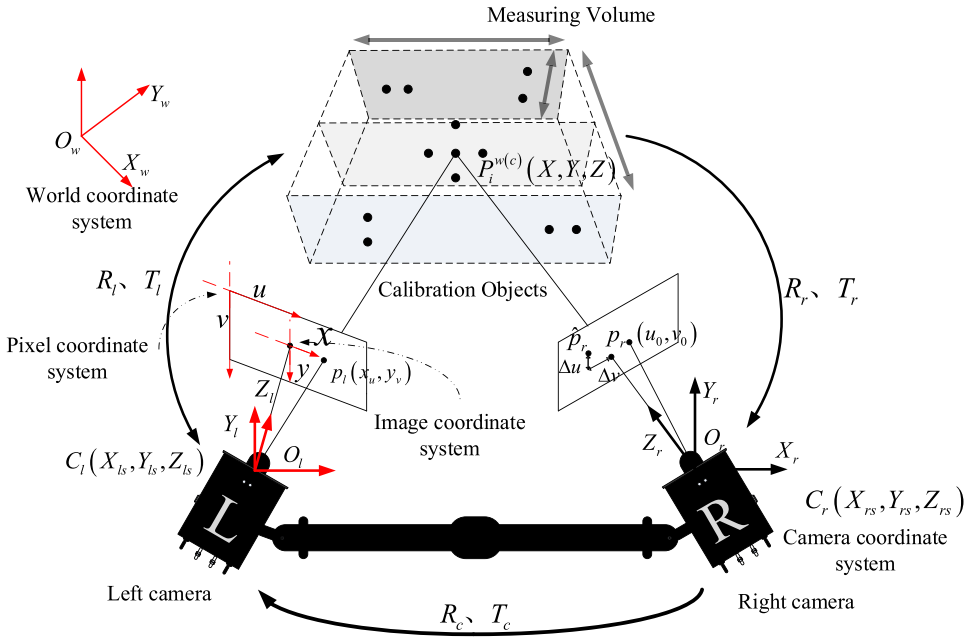

Fig. 1. Stereovision measurement system and imaging diagram.

environment reconstruction [16,17], etc.

Researchers [18] developed a set of golf stereo vision measurement and analysis system. The system can obtain the trajectory and speed of the ball by taking specially designed golf images. Through the analysis of the motion parameters of the ball, and then guide the players' batting action, realize the simulation training of the players, but the measurement accuracy is not high. Researchers [19,20] use two cameras fixed on the manipulator to take pictures of the feature pictures arranged in the environment, and locate the manipulator through the change of image features to obtain its motion parameters. And compared with the traditional manipulator that only relies on inertial parameters, by adding image features to the manipulator control, it can perform specific functions. Professor Helmick [21] has developed a Mars Lander based on stereo vision measurement technology. A pair of stereo vision cameras on the Rover are used to capture stereo image pairs. According to the change of image alignment features, the three-dimensional information of the rover is determined, and the real-time relative position and attitude parameters are obtained, and the motion trajectory is adjusted independently in the specific situation of the environment. Researchers [22] obtained the spatial environment characteristics through stereo vision camera, calculated its relative pose and motion state in virtual three-dimensional space, used for autonomous obstacle avoidance, trajectory planning and other space tasks, and also combined with other moving objects for assistance.

Vision measurement has a wide range of applications [23,24], with the advantages of simple method, principle and structure. However, most of the current visual motion measurement products are specially designed for specific measurement targets, there is no general measurement equipment, and the measurement accuracy is poor. Due to the difference of the measured object, the difference of function is considered in the design of the measurement system, and the measurement accuracy is ignored. At present, there is no universal vision measurement equipment. According to the particularity of moving objects in different fields, researchers in various countries in the world reasonably design the measurement scheme. According to the similarities and differences of the measured moving objects, they reasonably arrange the stereo vision motion measurement system and the differentiated attitude algorithm to complete the three-dimensional motion parameter measurement task of moving objects [25–27].

This paper will analyze the factors that affect the measurement accuracy of stereo vision, such as sensor layout, visual imaging model, single camera calibration, 3D reconstruction and so on. Firstly, the influence of the internal parameters of a single camera on the measurement results is analyzed, then the influence of the layout of binocular stereo vision measurement camera on the measurement results is analyzed, finally, the influence of the error caused by the measurement equivalent model on the measurement results is analyzed, and the whole measurement error solution model is given. According to the results of measurement error analysis, we design the experiment and analyze the results and evaluate accuracy of the system, so as to verify the correctness of this paper.

The remainder of this paper is organized as follows: In Section 2, we analyze the influence of intrinsic parameters on the calibration results and give the data-driven test results. In Section 3 and Section 4, we analyse the influence of the overall structure parameters and the camera external parameters on the measurement accuracy in stereo vision measurement, and give the error function to guide the parameter design of the measurement system. Meanwhile, we provide the experiments to examine the stereo vision measurement error function. In Section 5 gives the conclusion.

2. Camera calibration model and parameter analysis

2.1. Camera calibration model

Pinhole model is a widely used camera imaging model in computer vision. Imaging mapping involves the transformation between different coordinate systems. As shown in Fig. 1, the following coordinate systems are defined: the image coordinate system takes the upper left corner of the computer image as the origin, the horizontal and vertical axes are x and y directions respectively, and the unit is pixel; the image plane coordinate system takes the intersection O_C of the optical axis and the image plane as the origin, and the xy axis is the horizontal and vertical axes of the image plane respectively; the camera coordinate system takes the optical center O as the origin, and the optical axis is z axis, the xy axis is parallel to the horizontal and vertical axes of the image plane, and the world coordinate system is the reference system of three-dimensional space [28].

The ideal pinhole imaging model can be deduced. The mapping relationship between the coordinates of a space point in the world coordinate system $P_w(x_w, y_w, z_w)^T$and the coordinates of its projection point in the image coordinate system $p(u, v)^T$is:

$$z_c\begin{bmatrix} u \\ v \\ 1 \end{bmatrix} = \begin{bmatrix} f/d_x & \tau & c_x \\ 0 & f/d_y & c_y \\ 0 & 0 & 1 \end{bmatrix} \bullet \left\{ \mathbf{R} \bullet \begin{bmatrix} x_w \\ y_w \\ z_w \end{bmatrix} + \mathbf{T} \right\} = \mathbf{A} \bullet [\mathbf{R} \quad \mathbf{T}] \begin{bmatrix} x_w \\ y_w \\ z_w \\ 1 \end{bmatrix} \tag{1}$$

Wherein, $\mathbf{A}$ is the internal parameter matrix of the camera; $[\mathbf{R} \quad \mathbf{T}]$ is the external parameter matrix; f is the focal length of the camera; d_x, d_y are the horizontal and vertical spacing between CCD photosensitive elements; c_x, c_y are the coordinate of the main point; τ is the tilt factor(τ is 0 in general), indicating that the sensor chip is square; f_x is represented by f/d_x, f_y is f/d_y; z_c is the z coordinate value of the space point in the camera coordinate system. $\mathbf{R}$is a 3×3 rotation orthogonal matrix, it represents the rotation relationship between the camera coordinate system and the world coordinate system, $\mathbf{T}$is a 3×1 translation vector, representing the position relationship between the two coordinate systems.

In Fig. 1, the origin of the image coordinate system in the pixel coordinate system is (c_x, c_y), and the physical dimension of the unit pixel of the image plane in the x-axis and y-axis directions is d_x, d_y. Then, any image point in the image coordinate system $(u, v)$and its coordinate (x, y) in the image plane coordinate system satisfy the following relationship:

$$\begin{cases} u = \dfrac{x}{d_x} + c_x \\ v = \dfrac{y}{d_y} + c_y \end{cases} \tag{2}$$

It can be expressed as a matrix:

$$\begin{bmatrix} u \\ v \\ 1 \end{bmatrix} = \begin{bmatrix} 1/d_x & 0 & c_x \\ 0 & 1/d_y & c_y \\ 0 & 0 & 1 \end{bmatrix} \begin{bmatrix} x \\ y \\ 1 \end{bmatrix} \tag{3}$$

The inverse relation is:

$$\begin{bmatrix} x \\ y \\ 1 \end{bmatrix} = \begin{bmatrix} d_x & 0 & -c_x d_x \\ 0 & d_y & -c_y d_y \\ 0 & 0 & 1 \end{bmatrix} \begin{bmatrix} u \\ v \\ 1 \end{bmatrix} \tag{4}$$

Due to processing, installation and other reasons, the camera lens often has distortion, which makes the spatial projection not strictly comply with the perspective projection model, but has a certain degree of distortion. In this paper, the influence of radial distortion is mainly considered, and the distortion influence is transferred from the image plane pixel coordinate system to the image coordinate system. Let the ideal coordinate of the space point in the image plane coordinate system be (x, y) and the actual coordinate be (x_d, y_d). The corresponding formula (4) can be written as:

$$\begin{bmatrix} x_d \\ y_d \\ 1 \end{bmatrix} = \begin{bmatrix} d_x & 0 & -c_x d_x \\ 0 & d_y & -c_y d_y \\ 0 & 0 & 1 \end{bmatrix} \begin{bmatrix} u_d \\ v_d \\ 1 \end{bmatrix} \tag{5}$$

the relationship between them is as follows:

$$\begin{cases} x = x_d\left(1 + kr^2\right) \\ y = y_d\left(1 + kr^2\right) \end{cases} \tag{6}$$

In which, $r = \sqrt{x_d^2 + y_d^2}$, k is the primary radial distortion coefficient. Through formula (4), (5)and (6), we can get:

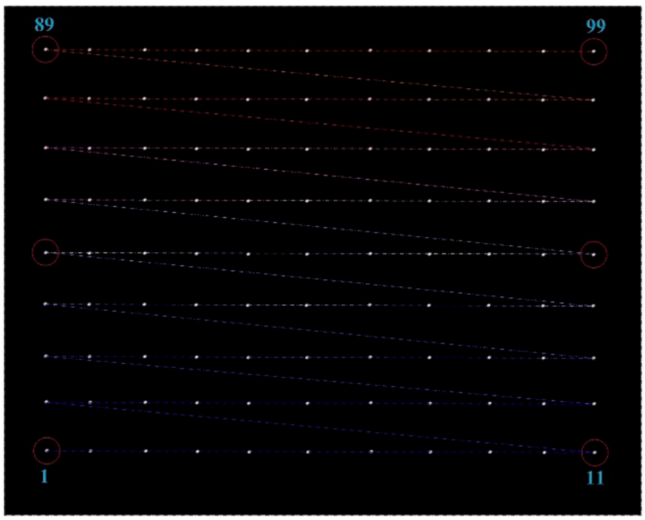

Fig. 2. Wall light points experimental images.

$$\begin{cases} x = x_d\left(1+kr^2\right) \\ y = y_d\left(1+kr^2\right) \end{cases} \Rightarrow \begin{cases} x = (u_d d_x - c_x d_x)\left[1+k\left(x_d^2+y_d^2\right)\right] \\ y = \left(v_d d_y - c_y d_y\right)\left[1+k\left(x_d^2+y_d^2\right)\right] \end{cases}$$
$$\Rightarrow \begin{cases} x = (u_d d_x - c_x d_x) + k\left(x_d^2+y_d^2\right)(u_d d_x - c_x d_x) \\ y = \left(v_d d_y - c_y d_y\right) + k\left(x_d^2+y_d^2\right)\left(v_d d_y - c_y d_y\right) \end{cases}$$
$$\Rightarrow \begin{cases} (ud_x - c_x d_x) = (u_d d_x - c_x d_x) + k\left(x_d^2+y_d^2\right)(u_d d_x - c_x d_x) \\ \left(vd_y - c_y d_y\right) = \left(v_d d_y - c_y d_y\right) + k\left(x_d^2+y_d^2\right)\left(v_d d_y - c_y d_y\right) \end{cases} \tag{7}$$
$$\Rightarrow \begin{cases} u = u_d + k \bullet \left[(u_d - c_x)^2 + \left(v_d - c_y\right)^2\right] d_x^2 \bullet (u_d - c_x) \\ v = v_d + k \bullet \left[(u_d - c_x)^2 + \left(v_d - c_y\right)^2\right] d_y^2 \bullet \left(v_d - c_y\right) \end{cases}$$

which, u_d, v_d are the projection coordinates after distortion, and u, v are the ideal projection coordinates. Formula (1) and (7) constitute the mapping relationship between the three-dimensional coordinates of space points and the image coordinates of their projection points. The main task of camera calibration is to find the internal and external parameter matrix **A**, **R**, **T** and distortion coefficient k.

Coplanar points are used for calibration, and the formula can be obtained by radial uniform constraint:

$$\begin{bmatrix} x_{wi}Y_{di} & y_{wi}Y_{di} & Y_{di} & -x_{wi}X_{di} & -y_{wi}X_{di} \end{bmatrix} \begin{bmatrix} r_1/T_y \\ r_2/T_y \\ T_x/T_y \\ r_4/T_y \\ r_5/T_y \end{bmatrix} = X_{di} \tag{8}$$

Considering that the global optimization of all calibration parameters is an effective means to improve the calibration accuracy [29, 30], we can establish the following optimization model:

$$\sum_{i=1}^{n} \left\| m_i - \breve{m}\left(\mathbf{R}, \mathbf{T}, s_x, k_1, f, C_x, C_y, M_i\right) \right\| \tag{9}$$

Where, $m_i$is the i-th world coordinate point in the calibration board, and M_i is the point corresponding to m_i on the pixel plane. $\breve{m}$ is the world coordinate point obtained by reverse calculation of M_i, it is a nonlinear minimization problem. We can use the values of the parameters obtained above as the initial value of the optimized solution and $k_1 = 0$, $s_x = 1$. The Levenberg-Marquardt method is used to solve all the parameters in the model.

2.2. Internal parameter analysis

In this paper, the effect of calibration points' numbers on the calibration parameters and results is tested by using the real image of laser points projected on the wall. The wall range is about 3 m × 4 m. Mikrotron MC3010 camera with resolution of 1690 × 1710, space between photosensitive elements, and lens model of AF zoom Nikkor 24-85 mm / 1:2.8–4d were used to take pictures of light spots on the wall. The points in the red circle in Fig. 2 are the initial six points participating in the calibration.

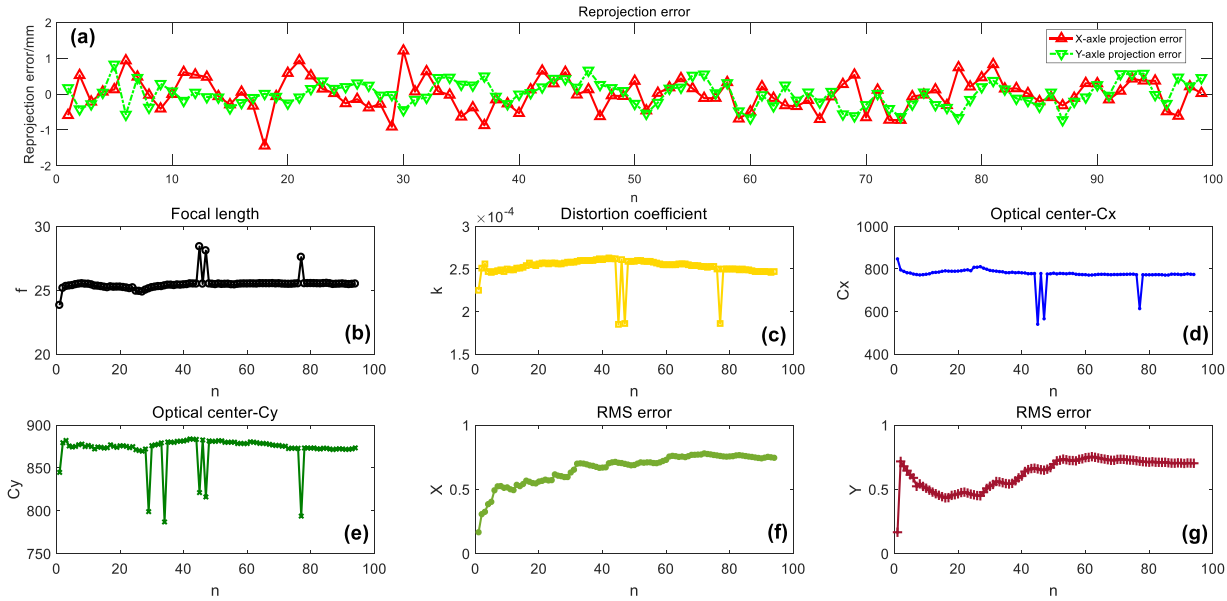

Fig. 3. The relationship between camera calibration points and internal parameters: (a) Reconstruction error with calibration points; (b) Focal length with calibration points; (c) Distortion coefficient with calibration points; (d) Optical center-C_x with calibration points; (e) Optical center-C_y with calibration points; (f) RMS in X direction with calibration points; (g) RMS in Y direction with calibration points.

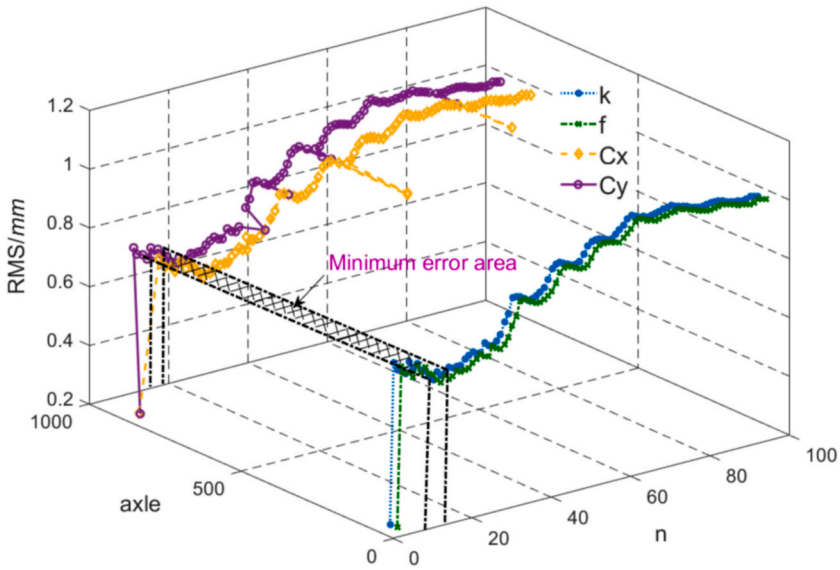

Fig. 4. The schematic of error changes the parameters under the unified axis.

The center coordinates of the circle are extracted by the barycenter method. Fig. 3 shows the relationship between the calibration result and the number of calibration points. It can be seen from the figure that the camera internal parameters will gradually stabilize at a certain value with the increase of the number of calibration points. The focal length$f$ and optical center (C_x, C_y)can be stabilized quickly, which shows that they are not sensitive to the number of calibration points, while the distortion coefficient is greatly affected by the number of calibration points.

Fig. 4 shows the effect of the number of calibration points on the calibration results by unifying the variation of each parameter into a coordinate axis. It can be seen from the figure that the calibration back projection error tends to a certain stable value after the number of calibration points reaches a certain number. From the figure, we can directly see the calibration points and the corresponding internal parameters in the area with the lowest back projection error.

Now analyze the influence of camera parameters on calibration error. According to Fig. 5, the change of focal length f has the greatest influence on the error, followed by the distortion coefficient and optical center. It shows that when the focal length f is stable,

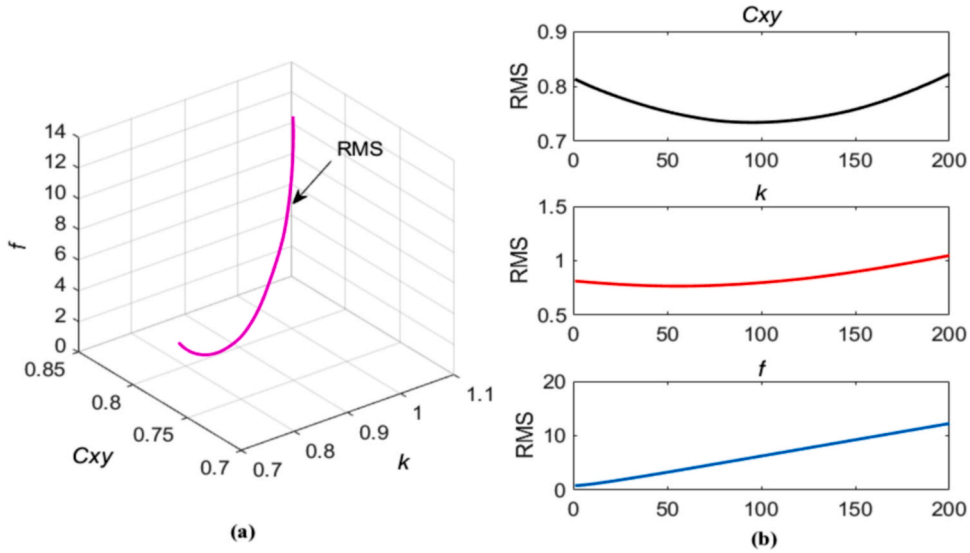

Fig. 5. The influence of camera internal changes to the calibration result: (a) unified error change; (b) normalized error change.

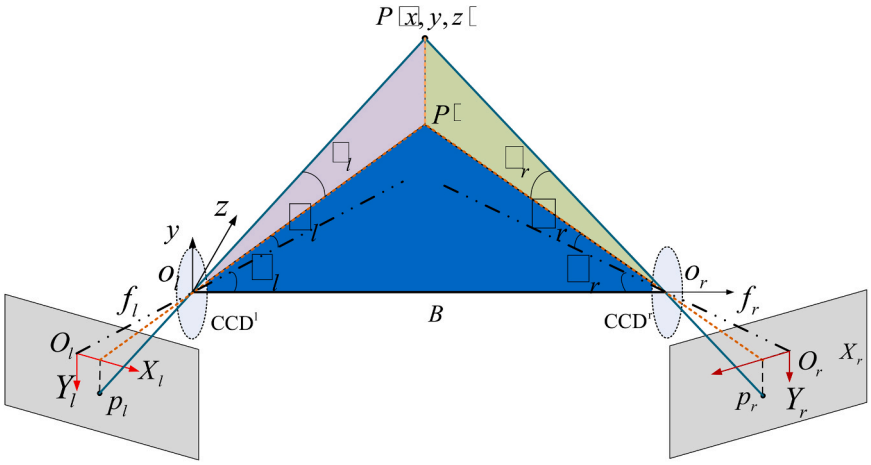

Fig. 6. Precision analysis model of cameras layout structure.

choosing the appropriate distortion coefficient k is beneficial to the calibration results.

3. Error analysis of external parameters in stereo vision measurement

3.1. Layout of stereo vision measuring cameras

The mathematical model of camera layout structure is shown in Fig. 6, including the angle (α_l, α_r) between baseline B and camera line of sight, focal length (f_l, f_r) and measuring distance$z$. The influence of these parameter changes on the measurement results is coupled and needs to be analyzed.

Suppose two cameras CCD^l and CCD^r are placed horizontally. The image coordinate system is represented by $O_l - X_l Y_l$ and $O_r - X_r Y_r$, $O_l o_l$ and $O_r o_r$ represent the optical axis of the left and right cameras respectively. The line connecting the two optical centers $o_l$and $o_r$is represented by B. The object point P is imaged in the left and right lenses, and is represented by $p_l(X_l, Y_l)$ and $p_r(X_r, Y_r)$ respectively. The measurement coordinate system is $o_l - x_l y_l z_l$, the projection of point P to the horizontal plane is represented by ω_l and ω_r, and the projection of point P to the vertical plane is represented by ϕ_l and ϕ_r. In the common view of the two cameras, the horizontal and vertical projections of the measured point are all in the camera field [31].

According to the geometric relationship shown in Fig. 6, point P can be expressed by camera layout structure parameters and projection angle. Let P' be the projection point of P on the horizontal plane. In $\triangle o_l o_r P'$ there are:

$$x = \cot(\omega_l + \alpha_l) \cdot z \tag{10}$$

$$\cot(\omega_l + \alpha_l) \cdot z + \cot(\omega_r + \alpha_r) \cdot z = B \tag{11}$$

Z is the z-axis value of P point in the measurement coordinate system, that is, the object distance. In$\triangle PP'o_l$, we can get:

$$\tan \phi_l = \frac{y \cdot \sin(\omega_l + \alpha_l)}{z} \tag{12}$$

The three-dimensional coordinates of point P can be expressed as:

$$\begin{cases} x = \dfrac{B \cot(\omega_l + \alpha_l)}{\cot(\omega_l + \alpha_l) + \cot(\omega_r + \alpha_r)} \\ y = \dfrac{z \tan \phi_l}{\sin(\omega_l + \alpha_l)} = \dfrac{z \tan \phi_r}{\sin(\omega_r + \alpha_r)} \\ z = \dfrac{B}{\cot(\omega_l + \alpha_l) + \cot(\omega_r + \alpha_r)} \end{cases} \tag{13}$$

In which, $\omega_l = \arctan\frac{X_l}{f_l}$, $\omega_r = \arctan\frac{X_r}{f_r}$, $\tan \phi_l = \frac{Y_1 \cdot \cos \omega_l}{f_l}$, $\tan \phi_r = \frac{Y_2 \cdot \cos \omega_r}{f_r}$.

The layout structure parameters of the camera are the key data, and the geometric relationship is shown in Fig. 6. Formula (13) can be expressed in the form of vector equation:

$$p(x, y, z) = F(B, \alpha_l, \alpha_r, f_l, f_r, X_l, X_r, Y_l, Y_r) \tag{14}$$

According to the theory of integrated distributed error, the overall error of 3D motion stereo vision measurement can be expressed as the measurement error of x, y and z axes:

$$\triangle = \sqrt{\triangle x^2 + \triangle y^2 + \triangle z^2} = \sqrt{\sum_i \sum_{x,y,z} \left(\frac{\partial F(x, y, z)}{\partial_i} \cdot \delta_i \right)^2} \tag{15}$$

Wherein δ is the error factor of each parameter. $\psi_i = \sqrt{\sum_{x,y,z} \left(\frac{\partial F(x,y,z)}{\partial_i} \right)^2}$ represents the error transfer function of each factor. Therefore, according to formula (13), the error transfer function of each coordinate point of the image can be expressed as:

$$\begin{cases} \dfrac{\partial x}{\partial X_l} = -\dfrac{B}{2f_l} \cdot \dfrac{\cos^2\omega_l \cdot \sin 2\theta_r}{\sin^2(\theta_l + \theta_r)} \\ \dfrac{\partial x}{\partial X_r} = -\dfrac{B}{2f_r} \cdot \dfrac{\cos^2\omega_r \cdot \sin 2\theta_l}{\sin^2(\theta_l + \theta_r)} \end{cases} \tag{16}$$

$$\begin{cases} \dfrac{\partial z}{\partial X_l} = -\dfrac{B}{f_l} \cdot \dfrac{\cos^2\omega_l \cdot \sin^2\theta_r}{\sin^2(\theta_l + \theta_r)} \\ \dfrac{\partial z}{\partial X_r} = -\dfrac{B}{f_r} \cdot \dfrac{\cos^2\omega_r \cdot \sin^2\theta_l}{\sin^2(\theta_l + \theta_r)} \end{cases} \tag{17}$$

$$\begin{cases} \dfrac{\partial y}{\partial Y_l} = \dfrac{B}{f_l} \cdot \dfrac{\cos \omega_l \cdot \sin \theta_r}{\sin(\theta_l + \theta_r)} \\ \dfrac{\partial y}{\partial Y_r} = \dfrac{B}{f_r} \cdot \dfrac{\cos \omega_r \cdot \sin \theta_r}{\sin(\theta_l + \theta_r)} \end{cases} \tag{18}$$

$$\begin{cases} \dfrac{\partial y}{\partial X_l} = -\dfrac{B}{f_l} \cdot \dfrac{\tan \phi_l \cos \omega_l \sin \theta_r}{\sin(\theta_l + \theta_r)\sin \theta_l} \left(\dfrac{\cos \omega_l \sin \theta_r}{\sin(\theta_l + \theta_r)} + \cos \alpha_l \right) \\ \dfrac{\partial y}{\partial X_r} = -\dfrac{B}{f_r} \cdot \dfrac{\tan \phi_r \cos \omega_r \sin \theta_r}{\sin(\theta_l + \theta_r)\sin \theta_r} \left(\dfrac{\cos \omega_r \sin \theta_l}{\sin(\theta_l + \theta_r)} + \cos \alpha_r \right) \end{cases} \tag{19}$$

In which , $\theta_l = \omega_l + \alpha_l$, $\theta_r = \omega_r + \alpha_r$.

3.2. External parameter analysis

3.2.1. The influence of angle (α_l, α_r) on measurement accuracy

3.2.1.a When$\alpha_l = \alpha_r = \alpha$The angle (α_l, α_r) between the two optical axes and the baseline is the key parameter to limit the relative position and attitude of the two cameras. The change of any angle is directly related to other parameters. In order to simplify the analysis process, it is assumed that the included angle $\omega_l = \omega_r = \omega$ on the horizontal projection plane, the image point error $\delta_X = \delta_Y =$

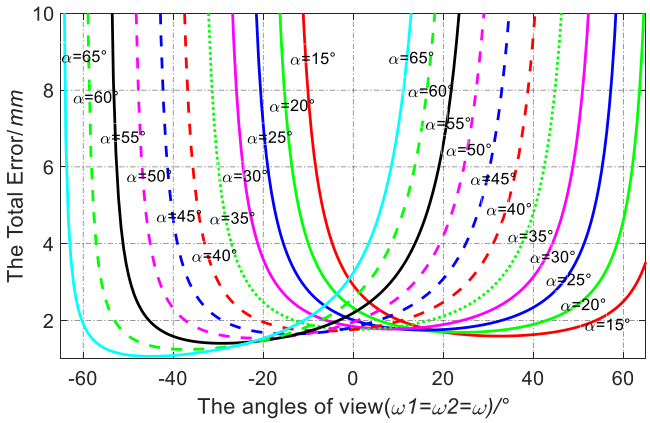

Fig. 7. The error distribution curve of the angle α.

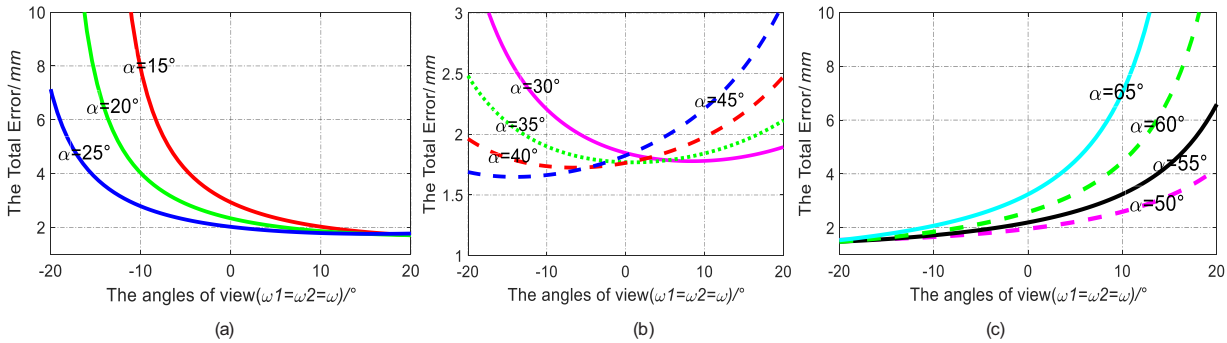

Fig. 8. The error distribution curve of the angle α with the ω= [− 20° 20°]: (a) The error curve of α_1; (b) The error curve of α_2(c) The error curve of α_3.

δ, the projection angle $\phi = \phi_l = \phi_r = 30^{\circ}$ on the vertical plane, and the measurement error of the coordinate point can be expressed as:

$$\triangle_{XY} = \frac{B\delta}{f} \cdot \frac{\sqrt{2}\cos\omega}{\sin 2\theta} \cdot \sqrt{\sin^2\theta + \frac{\cos^2\omega}{4\cos^2\theta} + \tan^2\phi\left(\frac{\cos\omega}{2\cos\theta} + \cos\alpha\right)^2} \tag{20}$$

In which , $\theta = \omega + \alpha$.

According to the error distribution Fig. 7, it can be seen that the measurement error changes gradually with the angle $\alpha(\alpha_l = \alpha_r)$ when ω= [− 65° 65°]. As the horizontal projection angle is positive and ω= [0° 20°],in the range of 15°≤α≤ 30°, the error distribution curve is inversely proportional to the intersection angle change; while in the range of 35°≤α≤ 65°, the error distribution curve is directly proportional to the intersection angle change; the error distribution curve is directly proportional to the intersection angle change when ω = [20° 65°]. As the horizontal projection angle is negative and ω= [- 20° 0°], in the range of 50°≤α≤ 65°, the error distribution curve is directly proportional to the intersection angle change; while in the range of 15°≤α≤ 45°, the error distribution curve is inversely proportional to the intersection angle change; the error distribution curve is inversely proportional to the intersection angle change when ω= [- 65–20°].

Considering the actual situation, the variation of measurement error with angle $\alpha(\alpha_l = \alpha_r)$ in the range of horizontal projection angle ω= [− 20° 20°] is analyzed. When the intersection angle $\alpha(\alpha_l = \alpha_r)$ changes in the interval [30° 45°], the measurement error function has a minimum value (as shown in Fig. 8b)). When the angle α> 45° and increases gradually, the measurement error increases with the increase of horizontal projection angle. When α> 45°, the measurement error increases sharply with the increase of α (as shown in Fig. 8c)). However, when α< 30°, the measurement error increases sharply with the decrease of α (as shown in Fig. 8a)).

To sum up, in order to balance the error distribution in the whole field of vision, the angle α is selected as the optimal angle in the interval [30° 60°] to ensure the minimum measurement error and the highest measurement accuracy.

3.2.1.b When$\alpha_l \neq \alpha_r$In fact, $\alpha_l = \alpha_r$ is a special state, and (α_l, α_r) is not necessarily equal due to the installation error and the need of the installation structure. The measurement error caused by $(\alpha_l, \alpha_r)$is:

$$\psi_{\alpha_l} = \frac{B\sin\theta_r}{\sin^2(\theta_l + \theta_r)} \sqrt{1 + \frac{\tan^2\phi_l}{\sin^2\theta_l} \cdot [\sin\theta_r - \sin(\theta_l + \theta_r)\cos\theta_l]^2} \tag{21}$$

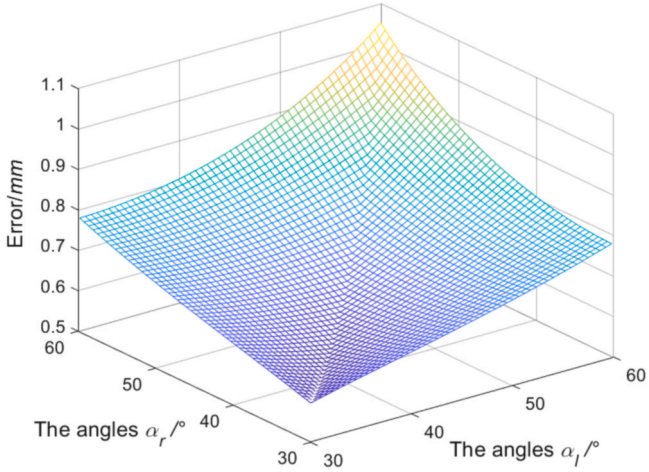

Fig. 9. The error distribution curve of two angles(α_l, α_r).

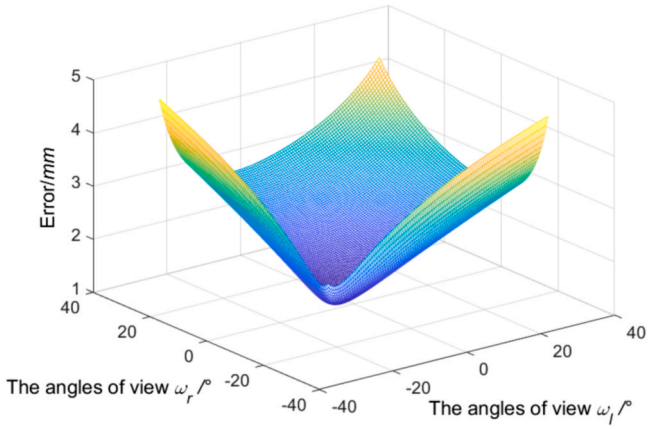

Fig. 10. The error distribution curve of the angles of view(ω_l, ω_r).

$$\psi_{\alpha_r} = \frac{B\sin\theta_l}{\sin^2(\theta_l+\theta_r)}\sqrt{1+\frac{\tan^2\phi_r}{\sin^2\theta_r}\cdot[\sin\theta_l - \sin(\theta_l+\theta_r)\cos\theta_r]^2} \tag{22}$$

Among them, $\theta_l = \omega_l + \alpha_l$, $\theta_r = \omega_r + \alpha_r$. When the angles (α_l,α_r)change at [30° 60°], the overall error changes accordingly. In this case, the total error is the maximum of two angle errors:

$$\psi_{\alpha_l \neq \alpha_r} = \max(\psi_{\alpha_l}, \psi_{\alpha_r}) \tag{23}$$

In Fig. 9, in the range of (α_l, α_r)= [30° 60°], $\omega_l = \omega_r$= 5° and $\phi_l = \phi_r$= 30°. When$\alpha_l = \alpha_r$, the error distribution is the minimum. Therefore, when the angle between the two parts increases gradually, the error also increases. The results shown in Fig. 9 prove the correctness of Fig. 7 and Fig. 8 again.

3.2.2. *The influence of the change of projection angle on the measurement accuracy*

As shown in Fig. 6, the horizontal projection angle(ω_l, ω_r) and the vertical projection angle(ϕ_l, ϕ_r) are the two projection angles of a point P, and the change of the projection angle affects the projection position of the point P. Assuming that the vertical projection angle is constant, the measurement error caused by the change of the object's position in the effective field of view with the horizontal projection angle is as follows:

$$\triangle_{\omega_1\omega_2} = \frac{B\delta}{f}\cdot\frac{1}{\sin^2(\theta_l+\theta_r)}\cdot\sqrt{\begin{array}{l}\cos^2\omega_l\sin^2\theta_r\left[\sin^2(\theta_l+\theta_r)+\cos^2\omega_l+\frac{\tan^2\phi_l}{\sin^2\theta_r}(\cos\omega_l\sin\theta_r+\sin(\theta_l+\theta_r)\cos\alpha_l)^2\right]+\\ \cos^2\omega_r\sin^2\theta_l\left[\sin^2(\theta_l+\theta_r)+\cos^2\omega_r+\frac{\tan^2\phi_r}{\sin^2\theta_r}(\cos\omega_r\sin\theta_l+\sin(\theta_l+\theta_r)\cos\alpha_r)^2\right]\end{array}} \tag{24}$$

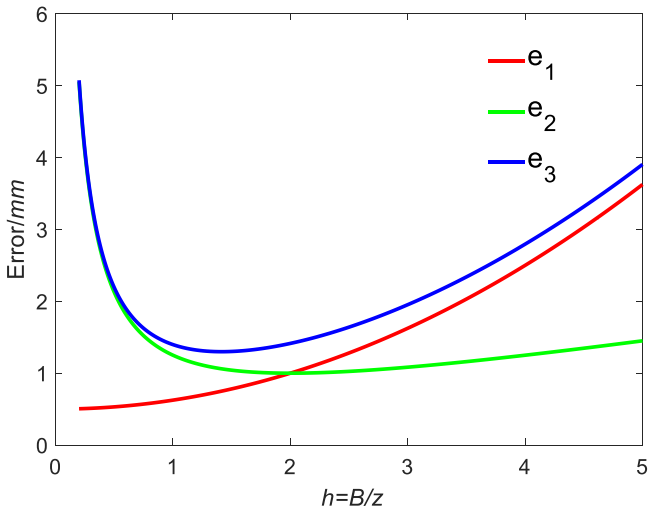

Fig. 11. The error distribution of the structural parameter $h = B/z$.

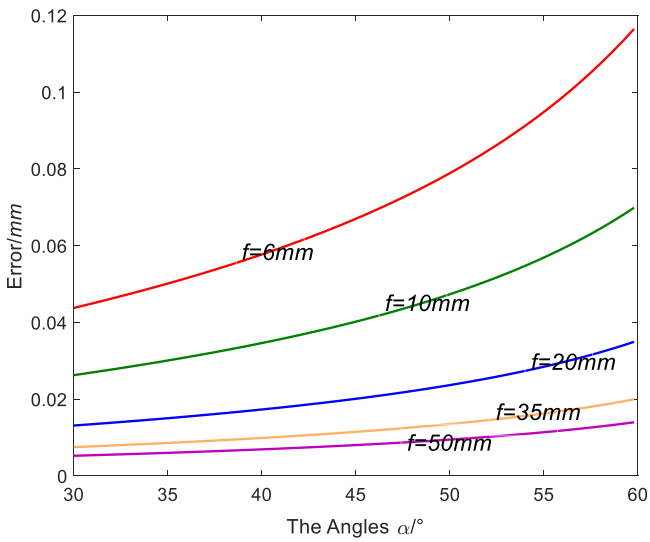

Fig. 12. The error distribution vary with the focus$f(f_l = f_r)$.

Wherein, $\theta_l = \omega_l + \alpha_l$, $\theta_r = \omega_r + \alpha_r$.

When$(\omega_l, \omega_r) = [-40^\circ\ 40^\circ]$, $\alpha_l = \alpha_r = 40^\circ$ and given $\phi_l = \phi_r = 30^\circ$, as shown in Fig. 10, the error distribution has a minimum value in the direction of equal projection angles. The error distribution tends to increase from the center of the view to the surrounding. It can be seen that the symmetrical distribution of the included angles can form the best camera layout and get the best measurement results.

3.2.3. *The Influence of baseline and object distance on measurement accuracy*

Baseline B is an important parameter to characterize the position of two cameras. Different baseline will affect the layout and measurement accuracy of the camera. When the baseline B changes, the angle(α_l, α_r) and object distance z will change accordingly. The focal length will also change with the change of object distance. In order to simplify the influence of baseline on measurement accuracy. We analyze the influence of the intersection of the two optical axes on the measurement accuracy, and approximate it as the impact of the baseline change on the accuracy. Suppose that the two cameras are symmetrically distributed on the horizontal plane, and$\alpha_l = \alpha_r = \alpha$, $\omega_l = \omega_r = 0$, $\phi_l = \phi_r = 0$. According to formula (13), we get:

$$\triangle_{Bz} = \sqrt{\triangle x^2 + \triangle z^2} = \sqrt{2}\ \frac{z\delta}{f} e_3 \tag{25}$$

Wherein, $e_1 = \frac{1}{h} \cdot \frac{\cot\alpha}{\sin^2\alpha} = \frac{1}{2} + \frac{1}{8}h^2$, $e_2 = \frac{1}{h} \cdot \frac{1}{\sin^2\alpha} = \frac{1}{h} + \frac{1}{4}h$, $e_3 = \sqrt{e_1^2 + e_2^2}$, and $h = \frac{B}{z} f_l = f_r = f$.

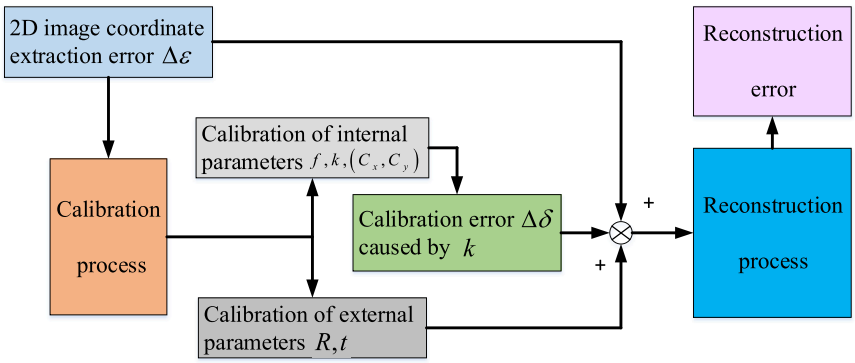

Fig. 13. Diagram of measurement error transfer.

For a given system, z, f, $\delta$is certain, so $\triangle_{Bz}$changes with e_3. The error distribution is shown in Fig. 11.

To sum up, $\triangle_{Bz}$changes in direct proportion with $e_1$ande_2, so the change trend $\triangle_{Bz}$ can be known throughe_3. As shown in Fig. 11, when the object distance z is fixed, the measurement error will increase with the baseline B. When the baseline is fixed, the measurement error will increase sharply with the object distance z. When the parameters h change in the open range (0.8 2.2), that is B= (0.8 2.2), the system measurement error is low. Therefore, when h< 0.5 or h> 3, that is B< 0.5z or B> 3z, it is necessary to adjust the camera layout structure according to the specific situation to reduce the error caused by the camera layout and improve the measurement accuracy.

3.2.4. *The influence of focal length on measurement accuracy*

Focal length is a very important parameter of lens, it represents the distance from optical center to imaging plane. We can select appropriate focal length by calculating the distance between measured object and camera, and considering the size of the field of view. In order to analyze the influence of focal length on measurement accuracy, the measurement error caused by focal length(f_l,f_r) of two cameras is obtained by using formula (13):

$$\zeta_{f_l} = \frac{B}{f_l}\frac{\sin\theta_r \sin\omega_l}{\sin(\theta_l+\theta_r)}\sqrt{\frac{\cos^2\omega_l}{\sin^2(\theta_l+\theta_r)}+\frac{\tan^2\phi_l}{\sin\theta_l}\cdot\left[cos\alpha_l-\frac{\sin\theta_r\cos\omega_l}{\sin(\theta_l+\theta_r)}-\frac{\sin\theta_l}{\sin\omega_l}\right]^2} \tag{26}$$

$$\zeta_{f_r} = \frac{B}{f_r}\frac{\sin\theta_l \sin\omega_r}{\sin(\theta_l+\theta_r)}\sqrt{\frac{\cos^2\omega_r}{\sin^2(\theta_l+\theta_r)}+\frac{\tan^2\phi_r}{\sin\theta_r}\cdot\left[cos\alpha_r-\frac{\sin\theta_l\cos\omega_r}{\sin(\theta_l+\theta_r)}-\frac{\sin\theta_r}{\sin\omega_r}\right]^2} \tag{27}$$

Among them, $\theta_l = \omega_l + \alpha_l$, $\theta_r = \omega_r + \alpha_r$.

In Fig. 12, $\omega_l = \omega_r = 5^\circ$ and $\phi_l = \phi_r = 30^\circ$ in the range of (α_l,α_r)= [30° 60°]. According to the error curve, the error decreases with the increase of focal length. If we refer to the conclusion in Fig. 10, we will find that the error increases with the increase of horizontal projection angle. It shows that the change of focal length is inversely proportional to the field of view and measurement error.The conclusion in Fig. 9 proves the correctness of the conclusion in Fig. 11, and also meets the imaging principle. So it shows that the focal length can be appropriately increased to improve the measurement accuracy in a specific environment.

4. Error analysis of stereo vision measurement and reconstruction

4.1. *The model of error analysis*

The error of vision measurement can be directly reflected by the error of 3D reconstruction. The process of 3D reconstruction is the process of reconstructing the 3D coordinates of the camera, which involves the camera calibration process. Camera calibration is to calculate the camera model parameters by knowing the 3D coordinates of a set of calibration points and their corresponding image coordinates. In the above two processes, image point coordinates are involved. The reconstruction error can be divided into the error caused by camera calibration process and the error of image coordinate extraction. The measurement error can be equivalent to the process shown in Fig. 13.

As can be seen from Fig. 13, the positioning error of the reconstructed spatial point is mainly affected by the 2D image coordinate extraction error of the target point and the camera calibration error. In order to facilitate the calculation, we use the calibrated distortion coefficient to reflect the size of the calibration error$\Delta\delta$, and$\Delta\varepsilon$is the 2D image coordinate extraction error, so the calibration error actually includes two parts, the 2D image coordinate extraction error and the image coordinate error caused by the distortion coefficient:

$$\Delta\delta = \frac{k^2(L/2)}{36} + \Delta\varepsilon \tag{28}$$

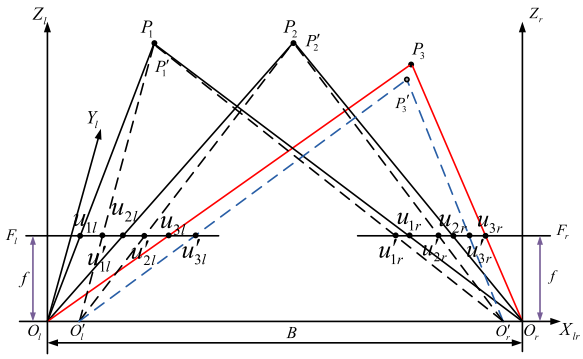

Fig. 14. Reconstruction error analysis model.

Where, L represents the diagonal of the imaging target plane by the image sensor and the k represent distortion coefficient calibrated by the camera.

Then, we analyze the spatial point reconstruction error caused by image coordinates. According to Fig. 1, we establish the following error analysis model of stereo vision measurement and reconstruction as shown in Fig. 14.$O_l$and$O_r$represent the optical centers of cameras l and r respectively.O_lZ_l and O_rZ_r represent the optical axis of the camera respectively. The two optical axes are parallel and the optical centers are B apart. The focal lengths of the two cameras are equal, both f. F is the imaging plane of the camera.

Establish the coordinate system $O-XYZ$, take O_l as the coordinate origin, take the line between $O_l$andO_r as the X axis, and take O_lZ_l as the Z axis. Thus, the optical center coordinates of the camera are $O_l(0,0,0)$, $O_r(0,0,B)$, and the image planes$F_l$and F_r are on the plane$Z=f$.

Taking P_1 point as an example, let its world coordinates be (x_w,y_w,z_w), and its image coordinates on the left and right images (x_l,y_l), (x_r,y_r) have the following relations. $y_w$is the same as x_w.

$$\begin{cases} \dfrac{x_l}{f}=\dfrac{x_w}{z_w} \\ \dfrac{B-x_r}{f}=\dfrac{B-x_w}{z_w} \end{cases} \Rightarrow \begin{cases} x_w=\dfrac{x_lB}{B+x_l-x_r} \\ z_w=\dfrac{fB}{B+x_l-x_r} \end{cases} \tag{29}$$

For the convenience of explanation, assume that P_1 andP_2 are the reference points, and their coordinates are(x_1,z_1),(x_2,z_2). For points P_1 and P_2, the ideal imaging positions are u_{11},u_{21}, and the actual positions obtained are u_{11}',u_{21}' according to the perspective projection model. We assume that the two-dimensional position errors of each pixel are equal, which is $\Delta\varepsilon$.According to the reference points P_1 and P_2, and the actual two-dimensional image points u_{11}',u_{21}' and u_{1r}',u_{2r}', we can calculate position of the camera optical center O_l' and O_r' by the linear geometric relationship. Then, the ideal imaging points u_{1l} and u_{2l} are obtained from the intersection of line $\overline{O_lP_1}$,$\overline{O_lP_2}$ and the camera imaging plane, which coordinates are$(fx_1/z,f)$,$(fx_2/z,f)$. Combining the two-dimensional position error $\Delta\varepsilon$ of pixel assumed previously, we can get the coordinates of u_{1l}' and u_{2l}' as $(fx_1/z+\Delta\varepsilon,f)$,$(fx_2/z+\Delta\varepsilon,f)$. Meanwhile, we can get the coordinates of point O_l' as $\left(\frac{z\Delta\varepsilon}{z-f},0\right)$ through lines $u_{1l}P_1'$and $u_{2l}P_2'$. Similarly, we can get the coordinates of the O_r'as$\left(B-\frac{z\Delta\varepsilon}{z-f},0\right)$.

The test point P_3 in Fig. 14 are reconstructed from the calculated camera model parameters. For the convenience, the coordinate of P_3 is set as(x_3,z_3), and the ideal imaging points on the two camera imaging planes are u_{3l},u_{3r}. Because of the camera model error and image point error of P_3, the imaging points are in u_{3l}',u_{3r}', and then the reconstruction point P_3' are obtained by perspective transformation of linear geometry.The coordinates of u_{3l},u_{3r} are $\left(\frac{fx_3}{z}+\Delta\varepsilon,f\right)$ and $\left(B-\frac{f(B-x_3)}{z}-\Delta\varepsilon,f\right)$ respectively. Set the camera calibration error as $\Delta\delta$. Then u_{3r}' coordinate is $\left(B-\frac{f(B-x_3)}{z}-\Delta\varepsilon-\Delta\delta,f\right)$. Therefore, the baseline length between O_l' and O_r' is $\left(B-2\frac{z\Delta\varepsilon}{z-f}\right)$, and the parallax d is $\frac{f(B-x_3)}{z}+\Delta\varepsilon+\Delta\delta+\left(\frac{fx_3}{z}+\Delta\varepsilon\right)-2\frac{z\Delta\varepsilon}{z-f}$. According to the relationship between left and right cameras, the world coordinate value of P_3'can be obtained.

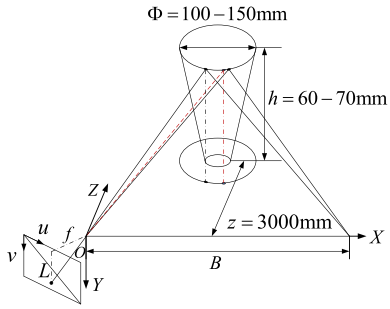

Fig. 15. Schematic diagram of measurement calculation.

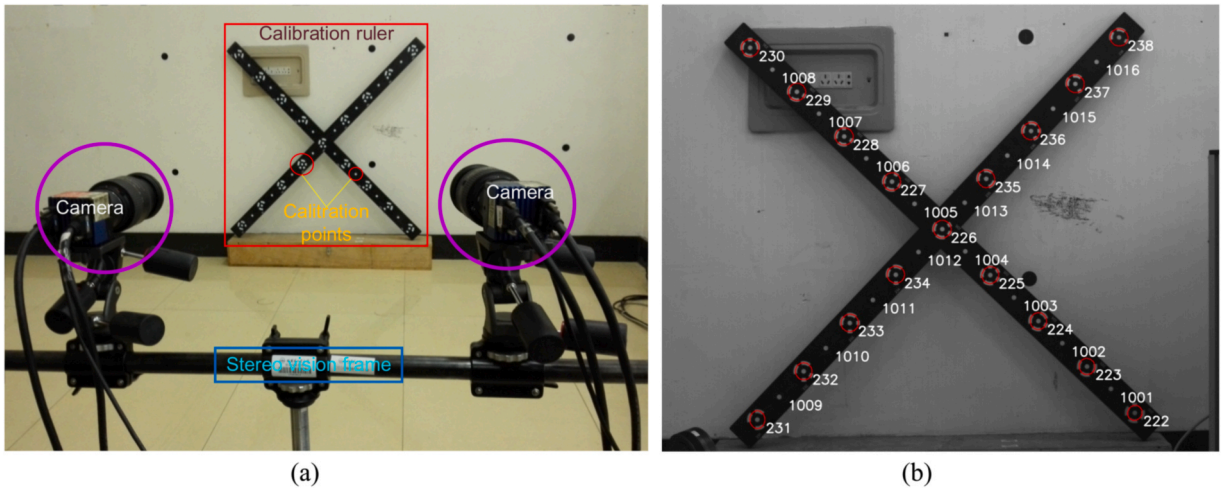

Fig. 16. Stereoscopic motion measurement system: (a) The system structure; (b) Target identification result.

$$\begin{cases} x_3' = \dfrac{\left(B - 2\dfrac{z\Delta\varepsilon}{z-f}\right)\left(\dfrac{fx_3}{z} + \Delta\varepsilon\right)}{\dfrac{f(B-x_3)}{z} + \Delta\varepsilon + \Delta\delta + \left(\dfrac{fx_3}{z} + \Delta\varepsilon\right) - 2\dfrac{z\Delta\varepsilon}{z-f}} \\ y_3' = \dfrac{\left(B - 2\dfrac{z\Delta\varepsilon}{z-f}\right)\left(\dfrac{fx_3}{z} + \Delta\varepsilon\right)}{\dfrac{f(B-x_3)}{z} + \Delta\varepsilon + \Delta\delta + \left(\dfrac{fx_3}{z} + \Delta\varepsilon\right) - 2\dfrac{z\Delta\varepsilon}{z-f}} \\ z_3' = \dfrac{\left(B - 2\dfrac{z\Delta\varepsilon}{z-f}\right)f}{\dfrac{f(B-x_3)}{z} + \Delta\varepsilon + \Delta\delta + \left(\dfrac{fx_3}{z} + \Delta\varepsilon\right) - 2\dfrac{z\Delta\varepsilon}{z-f}} \end{cases} \tag{30}$$

Then the measurement error formula is as follows:

$$error = \sqrt{|x' - x|^2 + |y' - y|^2 + |z' - z|^2} \tag{31}$$

4.2. Test and result analysis

According to the above analysis, 3D reconstruction is the calculation process of 3D coordinates of image points, which integrates the errors of camera calibration process. In fact, it is the reverse process of perspective imaging. When we solve the three-dimensional coordinates with known two-dimensional image point coordinates, there are many factors that affect the reliability and accuracy of the solution. Here, we assume that the camera has been calibrated and the calibration error is $\Delta\delta$, and the image coordinate error is $\Delta\varepsilon$.

The algorithm verification case is given: as shown in Fig. 15, according to the indicator requirements of the measured target, we configured the following measurement parameters, taking the measurement distance z = 3000 mm, the X direction distance of the

Table 1
The Main Parameters of the Test System.

Index	Parameters
Testing Environment	2 m × 2 m× 3 m
Left camera Parameters	$\mathbf{A}_l = \begin{bmatrix} 3107.561 & 0 & 825.846 \\ 0 & 3106.905 & 862.629 \\ 0 & 0 & 1 \end{bmatrix}, \mathbf{k}_l = [-0.1453 \quad 0.1179 \quad -0.0003 \quad -0.0002]^T$
Right camera Parameters	$\mathbf{A}_r = \begin{bmatrix} 3099.324 & 0 & 829.216 \\ 0 & 3086.258 & 806.371 \\ 0 & 0 & 1 \end{bmatrix}, \mathbf{k}_r = [-0.1381 \quad 0.1219 \quad 0.0003 \quad -0.0003]^T$
System parameter	$\mathbf{R}_{r2l} = \begin{bmatrix} 0.9937 & 0.0156 & 0.1928 \\ -0.0153 & 0.9996 & -0.0237 \\ -0.1931 & 0.0234 & 0.9928 \end{bmatrix}, \mathbf{T}_{r2l} = [-647.791 \quad 5.941 \quad 3.138]^T$
Calibration error	0.0871 mm
Reconstruction error	0.1092 mm

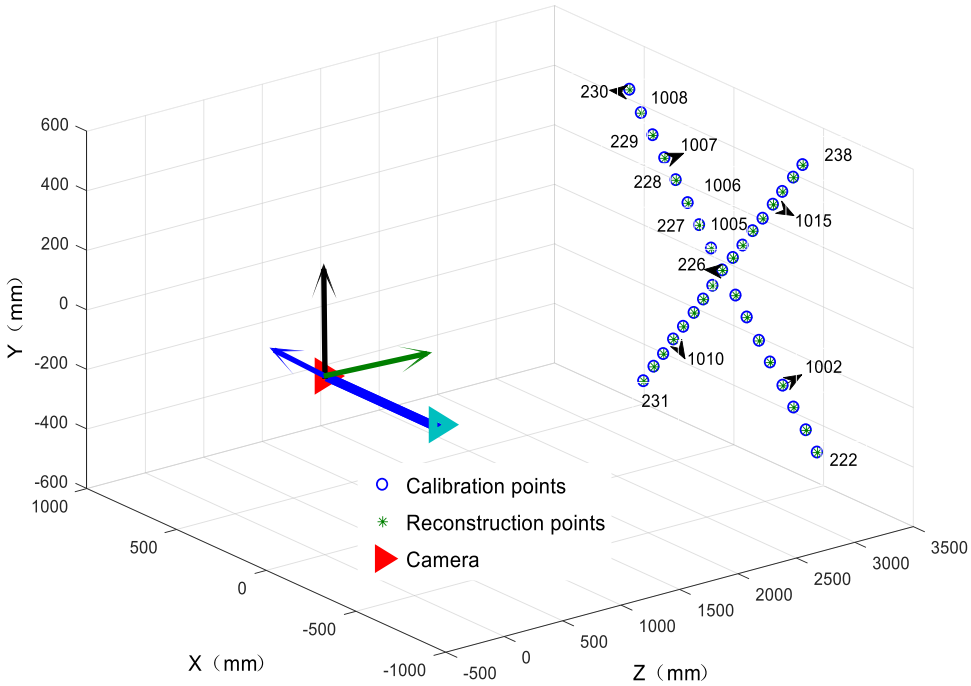

Fig. 17. The system reconstruction result.

measurement point x = 325 mm, the focal length f = 24 mm, the distortion coefficient k = 0.1, the baseline B = 650 mm, L = 19.2336 mm(resolution:1690 pixel×1710pixel), the image positioning error $\Delta\varepsilon$= 0.02pixel, the calibration error by formula (28), which is $\Delta\delta$= 0.0218pixel, and the camera pixel spacing d_x= 008 mm/pixel, according to formulas (30) and (31), we can calculate Δz= 0.1007 mm, Δx= 0.0091 mm, and the value $\Delta x$is equal to the valueΔy. The position error is:

$$error_p = \sqrt{\Delta x^2 + \Delta y^2 + \Delta z^2} = 0.1053 \text{ mm} \tag{32}$$

In the actual test, the stereo vision measurement system used in this paper is shown in Fig. 16, which is composed of two cameras and bracket. The camera parameters are consistent with the parameters in Section 2.2. The calibration target is a cross calibration ruler with coding characteristics, which can calibrate the measurement system.

In the testing process of stereo vision measurement system, the camera is calibrated according to the coordinates of image points. After calibrating the measurement system, image of the measured object is processed, and the left camera coordinate system is defined as the world coordinate system. According to the three-dimensional reconstruction principle of space points, the three-dimensional coordinates of each target point corresponding to the left camera coordinate system are calculated. The main test parameters of our vision measurement system obtained in this paper are shown in Table 1.

The above parameters from Table 1 refer to the test parameters given in the example. The calculated position error is in the same order of magnitude with the test result of the example, and it has at least one significant digit. Therefore, the stereo vision measurement error function established in this paper has a certain verification and guidance role for binocular stereo vision measurement camera calibration.

Table 2
The Target Reconstruction Results (unit: mm).

ID	Reconstructed coordinates			Relative center distance between 226		Error
	X	Y	Z	Reconstructed value	Exact value	
222	529.151	-390.023	3844.931	687.032	687.193	-0.161
1001	465.958	-330.276	3833.563	599.391	599.524	-0.133
223	407.082	-271.012	3820.666	514.865	515.002	-0.136
1002	346.514	-209.673	3805.944	427.42	427.426	-0.006
224	288.591	-149.653	3795.577	343.45	343.338	0.112
1003	226.993	-89.558	3779.295	255.892	256.012	-0.119
225	168.267	-30.553	3766.193	171.622	171.715	-0.092
1004	106.141	31.288	3751.878	82.803	82.83	-0.027
226	47.833	88.465	3738.182	0	0	0
1005	-18.713	157.986	3723.372	97.37	97.264	0.105
227	-77.3611	214.492	3712.967	179.422	179.51	-0.088
1006	-138.788	279.177	3696.324	270.093	269.954	0.139
228	-196.911	334.524	3682.215	351.535	351.422	0.113
1007	-258.028	398.728	3669.681	441.028	440.881	0.147
229	-316.779	454.848	3656.457	523.314	523.165	0.149
1008	-376.458	517.395	3641.366	611.046	610.965	0.081
230	-436.189	574.868	3628.535	694.901	694.747	0.153
231	529.402	572.555	3702.772	683.743	683.781	-0.037
1009	471.954	515.572	3708.493	602.644	602.507	0.136
232	407.548	451.621	3713.105	511.767	511.703	0.063
1010	348.992	393.553	3716.033	429.261	429.125	0.135
233	285.442	331.216	3721.954	340.072	339.962	0.109
1011	227.323	270.945	3725.757	256.261	256.164	0.096
234	163.445	210.727	3730.345	168.45	168.349	0.1
1012	105.783	151.262	3733.157	85.597	85.494	0.102
1013	-19.675	29.229	3742.692	89.926	89.961	-0.035
235	-81.022	-27.922	3746.541	173.838	173.839	0
1014	-140.88	-84.119	3750.151	256.01	256.109	-0.098
236	-204.351	-147.801	3754.037	345.933	345.8	0.133
1015	-262.483	-206.93	3759.686	428.972	428.866	0.106
237	-327.083	-267.384	3762.466	517.475	517.501	-0.026
1016	-385.021	-325.381	3765.418	599.477	599.598	-0.12
238	-449.846	-387.102	3770.244	689.111	689.229	-0.117

In order to further verify the analysis of this paper, in the three-dimensional reconstruction experiment of the cross target, the world coordinate is set in the left camera coordinate system, and two cross target images are taken with the calibrated measurement system. The center coordinate of the target point is extracted, and its spatial three-dimensional coordinates are calculated to reconstruct the cross target (as shown in Fig. 17), and compared with the accurately measured target data, Evaluate the measurement results. In order to better illustrate the effectiveness of the algorithm, the distance between the reconstruction point and the cross center of the target (code ID: 226) is used as the standard to test the accuracy of the measurement system. The results are shown in Table 2.

It can be seen from Table 2 that when the measurement distance is 3200–3800 mm, the average measurement error is 0.024 mm, the standard deviation is 0.107 mm, and the measurement accuracy is high. However, due to the lens distortion and the central point extraction error, the measurement accuracy of the edge point is relatively low, for example, the measurement error of No. 222 coding point is 0.161 mm. This proves the correctness of the error analysis of the stereo vision measurement system, and can be applied to different test conditions of stereo vision. Under the condition of the environment being measured, the accuracy of measurement can be given quickly to verify whether it can meet the measurement requirements. Under the condition of the required measurement accuracy, the configuration parameters suitable for the measurement requirements can be given.

5. Conclusions

In this paper, the measurement error of stereo vision is studied. Firstly, the relationship between the calibration parameters of a single camera and the measurement accuracy is analyzed, then the error caused by the camera layout of stereo vision measurement system is analyzed, and the optimal camera layout is given. Then, the reconstruction error caused by the equivalent model of three-dimensional motion stereo vision measurement is analyzed, and we give the calculation formula of reconstruction error in overall measurement, which can pre-calculate the measurement accuracy, and has a certain guiding role for the early design and sensor selection of vision measurement. Finally, the performance of the stereo vision measurement system is tested by examples and practical experiments. The test results verify the correctness of our stereo vision measurement error function studied in this paper, and provide theoretical guidance for the design of 3D motion stereo vision measurement system.

Declaration of Competing Interest

The authors declare that we have no financial and personal relationships with other people or organizations that can inappropriately influence our work, there is no professional or other personal interest of any nature or kind in any product, service and/or company that could be construed as influencing the position presented in, or the review of, the manuscript entitled.

Acknowledgements

This work was supported by the China Postdoctoral Science Foundation under Grant 2019M653870XB, National Natural Science Foundation of Shanxi Province under Grants No. 2020GY-003 and 2020JQ-292, National Natural Science Foundation of China under Grant 62001340 and Fundamental Research Funds for the Central Universities, China, XJS211306 and JC2007.

References

[1] S. Wang, Y. Xu, Y. Zheng, M. Zhu, H. Yao, Z. Xiao, Tracking a golf ball with high-speed stereo vision system, IEEE Trans. Instrum. Meas. 68 (8) (2019) 2742–2754.
[2] J.S. Cui, Y.H. Li, J. Huo, M. Yang, Y.K. Wang, Cong Li, A measurement method of motion parameters in aircraft ground tests using computer vision, Measurement 174 (108985) (2021).
[3] J. Peng, W. Xu, B. Liang, A. Wu, Pose measurement and motion estimation of space non-cooperative targets based on laser radar and stereo-vision fusion, IEEE Sens. J. 19 (8) (2019) 3008–3019.
[4] J.S. Cui, D.Z. Feng, C.W. Min, Q.C. Tian, Novel method of rocket nozzle motion parameters non-contact consistency measurement based on stereo vision, Optik 195 (163049) (2019).
[5] Z.Y. Jia, J.H. Yang, W. Liu, F.J. Wang, Y. Liu, L.L. Wang, C.N. Fan, K. Zhao, Improved camera calibration method based on perpendicularity compensation for binocular stereo vision measurement system, Opt. Express 23 (12) (2015) 15205–15223.
[6] M.L. Balter, A.I. Chen, T.J. Maguire, M.L. Yarmush, Adaptive kinematic control of a robotic venipuncture device based on stereo vision, ultrasound, and force guidance, IEEE Trans. Ind. Electron. 64 (2) (2017) 1626–1635.
[7] S.C. Lee, S.K. Hong, Velocity-aided attitude estimation for helicopter aircraft using microelectromechanical system inertial-measurement units, Sens. (Basel, Switz.) 16 (12) (2016) 2102.
[8] Z. Liu, S.N. Wu, Q. Wu, C.G. Quan, Y.M. Ren, A novel stereo vision measurement system using both line scan camera and frame camera, IEEE Trans. Instrum. Meas. 68 (10) (2019) 3563–3575.
[9] Y. Yang, Y. Que, S.Y. Huang, P. Lin, Multiple visual features measurement with gradient domain guided filtering for multisensor image fusion, IEEE Trans. Instrum. Meas. 66 (4) (2017) 691–703.
[10] L.Z. Zhang, D.M. Wu, Y.Q. Ren, Pose measurement for non-cooperative target based on visual information, IEEE Access 7 (2019) 106179–106194.
[11] S. Segal, A. Carmi, P. Gurfil, Stereovision-based estimation of relative dynamics between noncooperative satellites: theory and experiments, IEEE Trans. Contr. Syst. Technol. 22 (2) (2014) 568–584.
[12] D.M.K.K.V. Rao, Y.H. Wu, A vision-based navigation system for perching aircraft, J. Intell. Robot Syst. 95 (2019) 555–566.
[13] B.H. Shan, W.T. Yuan, H. Wang, Z.X. Zuo, S. Li, Stereovision monitoring for entire collapse of a three-story frame model under earthquake excitation, Struct. Control Health Monit. 25 (6) (2018), e2161.
[14] W. Song, Y. Yang, M. Fu, F. Qiu, M. Wang, Real-time obstacles detection and status classification for collision warning in a vehicle active safety system, IEEE Trans. Intell. Transp. Syst. 19 (3) (2018) 758–773.
[15] Y. Lu, D. Song, Visual navigation using heterogeneous landmarks and unsupervised geometric constraints, IEEE Trans. Robot. 31 (3) (2015) 736–749.
[16] A. Ahmadi, F. Destelle, L. Unzueta, D.S. Monaghan, M.T. Linaza, K. Moran, N.E. O'Connor, 3D human gait reconstruction and monitoring using body-worn inertial sensors and kinematic modeling, IEEE Sens. J. 16 (24) (2016) 8823–8831.
[17] X.W. Li, Y. Wang, Q. Li, Q.H. Wang, J.Z. Li, S.T. Kim, Xin Zhou, Optical 3D object security and reconstruction using pixel-evaluated integral imaging algorithm, Opt. Express 27 (15) (2019) 20720–20733.
[18] U. Johansson, R. König, P. Brattberg, A. Dahlbom, and M. Riveiro, "Mining trackman golf data," in Proc. Int. Conf. Comput. Sci. Comput. Intell. (CSCI), Las Vegas, NV, USA, Dec. 2015, pp. 380–385.
[19] T.S. Huang, A.N. Netravali, Motion and structure from feature correspondences: a review, Proc. IEEE 82 (2) (1994) 252–268.
[20] J. Weng, T.S. Huang, N. Ahuja, Motion and structure from two perspective views: algorithms, error analysis, and error estimation, IEEE Trans. Pattern Anal. Mach. Intell. 11 (5) (1989) 451–476.
[21] D.M. Helmick, Yang Cheng, D.S. Clouse, M. Bajracharya, L.H. Matthies and S.I. Roumeliotis, "Slip compensation for a Mars rover," in Proc. IEEE/RSJ Int. Conf. Intell. Robot. Syst., Edmonton, Alta., 2005, pp. 2806–2813.
[22] S. Tijmons, G.C.H.E. de Croon, B.D.W. Remes, C. De Wagter, M. Mulder, Obstacle Avoidance Strategy using Onboard Stereo Vision on a Flapping Wing MAV, IEEE Trans. Robot. 33 (4) (2017) 858–874.
[23] D.L. Zhao, F.F. Kong, F.Z. Du, Feature Extraction for Incomplete Data Via Low-Rank Tensor Decomposition With Feature Regularization, IEEE Trans. Neural Netw. Learn Syst. 30 (10) (2019) 1803–1817.
[24] N. Murmu, B. Chakraborty, D. Nandi, Relative velocity measurement using low cost single camera-based stereo vision system, Measurement 141 (2019) 1–11.
[25] H.P. Zhang, Z.G. Jiang, A. Elgammal, Vision-based pose estimation for cooperative space objects, Acta Astronaut 91 (10–11) (2013) 115–122.
[26] J.H. Sun, Y. Zhang, X.Q. Cheng, A high precision 3D reconstruction method for bend tube axis based on binocular stereo vision, Opt. Express 27 (3) (2019) 2292–2304.
[27] V. Pesce, M. Lavagna, R. Bevilacqua, Stereovision-based pose and inertia estimation of unknown and uncooperative space objects, Adv. Space Res. 59 (1) (2017) 236–251.
[28] J.S. Cui, C.W. Min, X.Y. Bai, J. Cui, Exogenous biological renal support ameliorates renal pathology after ischemia reperfusion injury in elderly mice, Aging (Albany NY) 11 (2) (2019) 2031–2044.
[29] L.R. Ramírez-Hernández, J.C. Rodríguez-Quiñonez, M.J. Castro-Toscano, D. Hernández-Balbuena, W. Flores-Fuentes, R. Rascón-Carmona, L. Lindner, O. Sergiyenko, Improve three-dimensional point localization accuracy in stereo vision systems using a novel camera calibration method, p.1729881419896717: 1-15, Int. J. Adv. Robot. Syst. 17 (1) (2020), 172988141989671.
[30] Z.Y. Zhang, A flexible new technique for camera calibration, IEEE Trans. Pat. Anal. Mach. Intell. 22 (11) (2000) 1330–1334.
[31] Q. Liu, X.S. Qin, S.S. Yin and F. He, Structural parameters optimal design and accuracy analysis for binocular vision measure system, in Proc. IEEE/ASME Int. Conf. Adv. Intell. Mech., 2008, pp 156–161.